Available online at www.sciencedirect.com
jmr&t Journal of Materials Research and Technology
journal homepage: www.elsevier.com/locate/jmrt

Chemical-mineralogical characterization of critical elements into ferromanganese crusts

Caroline Silva de Matos [a,b], Mariana Benites [b], Luigi Jovane [b], Carina Ulsen [a,*]

[a] Department of Mining and Petroleum Engineering, Universidade de São Paulo, Brazil
[b] Department of Physical, Chemical, and Geological Oceanography, Universidade de São Paulo, Brazil

ARTICLE INFO

Article history:
Received 28 April 2023
Accepted 3 July 2023
Available online 6 July 2023

Keywords:
Ferromanganese crusts
Technological characterization
Deep sea mining
Critical metals
Manganese oxides

ABSTRACT

The demand for critical chemical elements applied in clean energy technologies is increasing and, although deep-sea mining feasibility still is an open question, it might be a pathway to overcome the problem. Among areas of interest for seabed mining, the Rio Grande Rise is an ocean ridge in the southwest Atlantic Ocean known for hosting a large polymetallic mineral deposit containing various critical elements at high concentrations. Therefore, this mineralogical and chemical study characterizes the Rio Grande Rise FeMn crusts and establishes features from a structural-chemical perspective that can guide further studies from various locations. Combining X-ray diffractometry, Raman spectroscopy, chemical analysis, and Scanning Electron Microscopy, it was found that samples are composed by manganese oxides, MnO_x; ferryxite or goethite, FeOOH; magnesian calcite, $Ca,Mg(CO_3)_2$; and carbonate fluorapatite, $Ca_5(PO_4,CO_3)_3F$. The external portion of analyzed rocks consists of younger crust layers enriched in critical metals, such as cobalt (Co) and nickel (Ni), associated with MnO_x – mainly vernadite and asbolane; titanium (Ti), associated with iron oxyhydroxides; and rare earth elements (REE), at distinct bearing minerals. Therefore, the data herein reported show that regions where the FeMn crusts have a thicker young layer host a higher content of critical elements. In addition, the information about the elemental distribution and mineral associations can guide further mineral and metallurgical processing steps.

© 2023 The Authors. Published by Elsevier B.V. This is an open access article under the CC BY-NC-ND license (http://creativecommons.org/licenses/by-nc-nd/4.0/).

1. Introduction

Climate change horizon unleashed the search and development of new technologies to provide cleaner energy and sustainable industrial production. Under this scope, the implementation and expansion of devices for energy supply such as solar cells, wind turbines, and batteries for electric vehicles have collaborated with an increasing demand for critical minerals and associated chemical elements [1]. A mineral is classified as critical when it is a source of an essential chemical element for a specific technological application, but its supply is at risk due to any extraction, processing, or political limitations [2]. Taking into account the clean energy industry, critical elements include transition metals such as cobalt (Co), manganese (Mn), and nickel (Ni); and the lanthanides, yttrium (Y) and scandium (Sc), known as rare earth elements (REE) [3]. According to the International

* Corresponding author.
E-mail address: carina.ulsen@usp.br (C. Ulsen).
https://doi.org/10.1016/j.jmrt.2023.07.021
2238-7854/© 2023 The Authors. Published by Elsevier B.V. This is an open access article under the CC BY-NC-ND license (http://creativecommons.org/licenses/by-nc-nd/4.0/).

Energy Agency [2], in the most optimistic future scenario the global demand for critical minerals is going to increase from 7 $\times$ 10^6 tons yr^{-1} in 2021 to 13 $\times$ 10^6 tons yr^{-1} in 2050. The main concern about these growing demands relies on the fact that many elements are pivotal for clean energy technologies (Table 1). The production of those elements is concentrated in a few countries, limited to their production capacity. Moreover, many mineable regions are located in regions culturally important to native peoples or threatened by water, food, and conflict insecurity [3–5].

Therefore, deep-sea mining emerges as a new pathway to increase the global extraction of critical minerals and supply the clean energy industry's needs [6,7]. Although there is a broad debate encompassing mineral exploitation versus environmental impact [8,9], scientific research can provide a better answer on mitigating impacts in cost-effective mining seabed. That is why recognizing potential areas for exploitation as well as critical metals content and their mineral association is so important.

Ferromanganese (FeMn) crusts are sedimentary authigenic mineral deposits containing manganese oxides and iron oxyhydroxides deposited onto the external and internal surface of hard substrates [10–12], although few studies report their occurrence in soft surfaces [13,14]. The FeMn crusts are widely known to contain a large variety and high content of metals, standing out as one of the most important mineral resources accessed by deep-sea mining. In particular, FeMn crusts are enriched in critical elements such as Co, Ni, Te, Platinum Group Metals (PGMs), and REE [11]. Usually found at submarine elevations at a water depth ranging from 400 m to 7 km [11], FeMn crusts form upon the seafloor surface by slow precipitation (few millimeters per million-year, mm Ma^{-1}) of colloidal particles of MnO_2 and FeOOH containing adsorbed species from seawater, in a process called hydrogenesis [10]. Thus, seawater chemical composition, influenced by nearby volcanic activity, biological production, and consumption, as well as riverine and atmospheric dust inputs, has a critical influence on FeMn crusts [6]. Still, post-depositional processes, such as redox chemical reactions and phosphatization events can modify the mineral and chemical composition of the crusts [15].

Considering all the factors aforementioned, the concentration of critical chemical elements in FeMn crusts depends on their geographical localization [10]. Among known areas containing FeMn crusts, the most studied and prominent from the exploration point of view is the Pacific Prime Crust Zone (PPCZ) in the Pacific Ocean [10]. The region contains one of the oldest FeMn crusts that have concentrated high amounts of critical metals in about 7.5 gigatons of dry sediment [16]. Although much knowledge concerning FeMn crust deposits in the Pacific, Indian, and Northeast Atlantic Oceans has been accumulated in the past decades, there is still a huge lack of information about regions in the South Atlantic Ocean, such as the Rio Grande Rise (RGR) [11,17,18].

The RGR is an ocean ridge located in the southwest Atlantic Ocean at around 1200 km from the Brazilian southeast coast [19]. Although an exploration contract for FeMn crusts in this region was regulated between the International Seabed Authority and the Geological Survey of Brazil since 2015, only recently scientific investigation studied the mineralogical and chemical composition of the crusts. Unprecedented mineralogical, geochemical, and isotopic characterization of 22 samples from the summit of RGR (shallow-water, 650–825 m) revealed the content of critical metals Ni, Co, REE, and Ti were 0.30–1.10 %wt, 0.09–0.79 %wt, 138–2821 ppm, and 0.05–0.09 % wt, respectively [17]. Sousa et al. [20] reported the petrographic, mineralogical, and chemical analysis of other 14 samples from RGR which the content of Ni, Co, REE, and Ti ranged between 0.29 and 0.68 %wt, 0.21–1.05 %wt, 675–2841 ppm, and 0.38–1.24 %wt, respectively. Both studies described the presence of two generations of FeMn crust with a distinct appearance, mineralogy, and chemical composition in the RGR: (1) an older generation (48–55 Ma) composed of 10 Å manganates, calcite, and carbonate fluorapatite as a result of strong diagenetic phosphatization covered by (2) a younger generation (less than 6 Ma), non-phosphatized, composed of vernadite and Fe-oxyhydroxides [17,20]. FeMn crusts phosphatization (shallower than 1500 m) occurred in relation to suboxic conditions developed in the Middle Miocene Climatic Optimum, so deeper than 1500 m crusts are not affected by phosphatization and do not have those different generations. Additionally, the history and mechanism of phosphatization of the FeMn first-generation were investigated by Benites et al. [15].

The identification of mineral phases based exclusively on X-ray diffraction, as reported in previous studies in the RGR, is limited to crystalline phases at concentrations higher than the detection limit (around 3%); moreover, do not differentiate similar patterns of diverse manganates due to their poor crystallinity and isomorphic substitution into the lattice. Therefore, this study focused for the first time on a structural perspective applying Raman spectroscopy as a tool to improve FeMn crust characterization in the RGR. This encompasses the compositional characterization of 9 bulk samples from RGR, comparing structural and chemical aspects of the older and younger crust layers. Besides expanding the number of analyzed samples from this region, our proposal comprises deepening the understanding of compositional and structural aspects of minerals to support further decision-making in minerals exploitation.

2. Materials and methods

2.1. Samples

The FeMn crust samples analyzed (9 samples, Fig. 1) were dredged from RGR between 650 and 825 m water depths (Fig. 2, Table 2) during the scientific cruise RGR1 on board the N/Oc Alpha Crucis of the Instituto Oceanográfico of Universidade de São Paulo (more information about the cruise was previously reported [21]). The samples were named according to the dredge number (D02, D05, D06, D07, D09, and D10) and their corresponding number ID within the dredge (030, 011, etc.). Original samples were cut still on board and subsampled in land. The younger layer of sample D07_006 was detached from the older surface, and treated as an independent sample (D07_006_0).

From each of the sample fragments, two smaller pieces were cut. The first one was ground for X-ray diffractometry

Table 1 – High (■■■), moderate (■■), and low (■) need of some chemical elements for developing clean energy technologies, adapted from [2]. PGM refers to the platinum group metals (ruthenium, rhodium, palladium, osmium, iridium e platinum).

Clean energy technology	Cu	Co	Ni	REE	Cr	Zn	PGMs
Solar Photovoltaic	■■■	■	■	■	■	■	■
Wind	■■■	■	■■	■■■	■■	■■■	■
Concentrating solar power	■■	■	■■	■	■■■	■■	■
Bioenergy	■■■	■	■	■	■	■■	■
Geothermal	■	■	■■■	■	■■■	■	■
Nuclear	■■	■	■■	■	■■	■	■
Electricity networks	■■■	■	■	■	■	■	■
Electric vehicles and batteries	■■■	■■■	■■■	■■■	■	■	■
Hydrogen	■	■	■■■	■■	■	■	■■■

and chemical analysis in an agate vase using a Fritsch Pulverisette 5 high-energy planetary mill for 10 min, according to the standard procedure of the Technological Characterization Laboratory (Department of Mining and Petroleum Engineering, Polytechnic School, Universidade de São Paulo) (Fig. S1); the second was used for Raman spectra register and further prepared for Scanning electron microscopy (SEM) analysis for samples D07_002, D07_006_0 and D10_002 (Fig. S2).

2.2. *Characterization*

Powder X-ray diffractograms (PXRD) were recorded in a Malvern Panalytical Empyrean 3rd generation diffractometer, using a Cu Kα radiation ($\lambda = 1.542$ Å, 45 kV and 40 mA) in 2θ range from 2.5 to 70° and a step of 0.02° s^{-1}.

Raman spectra were collected from pristine rock fragments in a Renishaw Invia Reflex spectrometer, equipped with a CCD camera (1040 x 256 pixels) thermoelectrically cooled detector and coupled to a Leica DM2500 M optical microscope (50x lens). Excitation was performed using a diode laser (λ_{ex} of 785 nm, power of 0.5 mW) and a diffraction grating of 1200 lines.

Chemical analysis of major elements was performed in a Malvern Panalytical Zetium X-ray fluorescence spectrometer at the Technological Characterization Laboratory using fused beads with lithium tetraborate as flux and powdered samples in a mass ratio of 7:1 (flux:sample). The analytical method was standardless for chemical elements between fluorine (F) and uranium (U), and the obtained concentrations (%wt) were normalized to 100%. Loss on ignition (LOI) was determined from sample calcination at 1020 °C for 2 h. Minor and trace elements, including lithium (Li), yttrium (Y), rare earth elements (REE), zirconium (Zr), niobium (Nb), barium (Ba), hafnium (Hf), tantalum (Ta), tungsten (W), lead (Pb), thorium

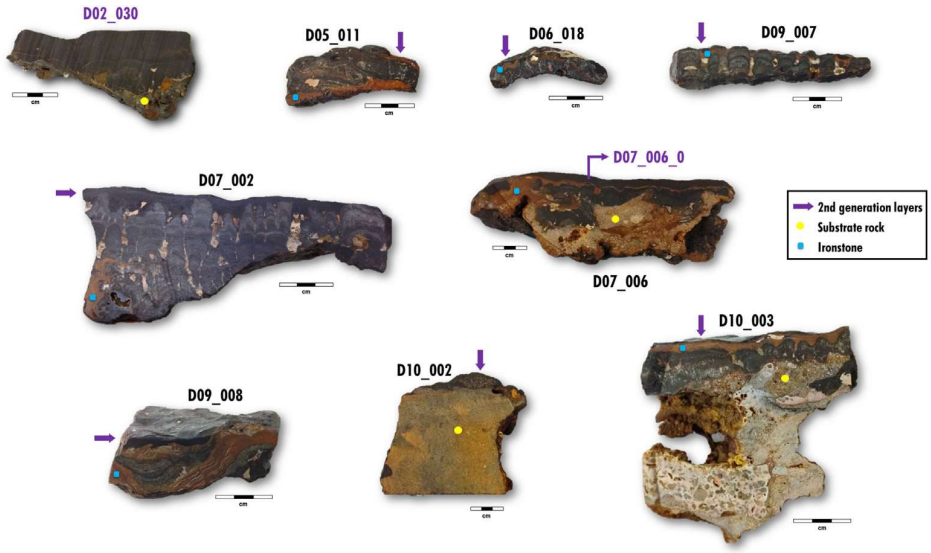

Fig. 1 – FeMn crust samples from RGR.

(Th) and uranium (U), were analyzed by Inductively Coupled Plasma Mass Spectrometry (ICP-MS) at Laboratoratório de Química e ICP-MS, Geoanalítica - Universidade de São Paulo Facility under method established by Navarro et al. [22]. Based on chemical analysis, a correlation matrix was generated in Origin® 2021 software to evaluate Spearman coefficients (R-value) at a confidence level of 95%.

Rock fragments of samples D07_002, D07_006_0, and D10_002 were mounted and embedded into epoxy resin and polished to obtain flat sections (Fig. S3). The sections were analyzed in a Quanta 650 FEG (Thermo Fisher/FEI) SEM microscope coupled to a Quantax 4030 (Bruker) energy-dispersive X-ray spectrometer (EDS) for chemical elemental mapping and punctual spectra acquisition.

3. Results and discussion

3.1. *Structural characterization*

3.1.1. *Powder X-ray diffraction*

PXRD pattern of FeMn crusts presented in this study (Fig. 3) correspond to the presence of specific diffraction peaks associated with manganese oxides (MnO_x), iron oxyhydroxide

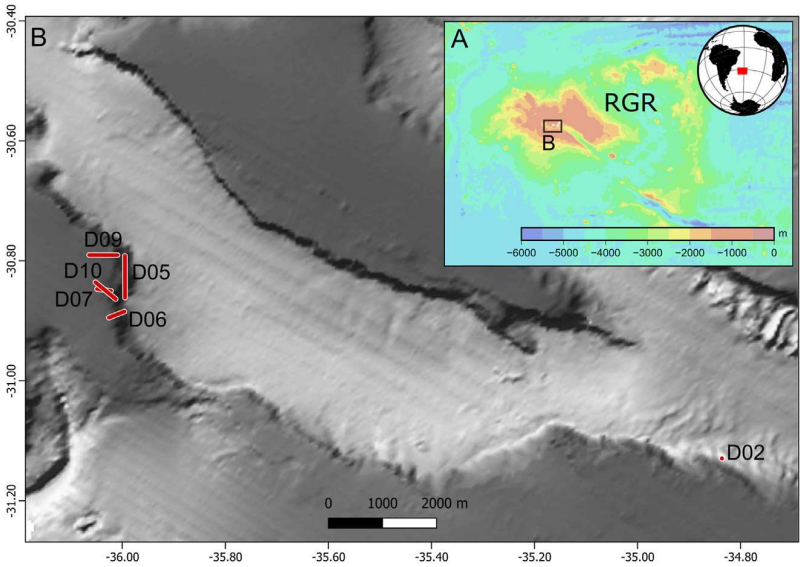

Fig. 2 – Geographical location and bathymetric map of RGR (a) showing the surveyed area (b), in which dredged areas are indicated by red traces.

Table 2 – Geographical coordinates and depths of initial and final survey points conducted by dredging (bold indicates final points).

Sample	Latitude	Longitude	Depth (m)
D02_030	31°09.365′S	34°49.800′W	851
	31°09.337′S	**34°49.807′W**	**800**
D05_011	30°47.782′S	35°58.795′W	683
	30°58.952′S	**35°58.912′W**	**795**
D06_018	30°53.346′S	35°59.029′W	741
	30°53.922′S	**36°00.836′W**	**692**
D07_002	30°51.251′S	36°00.519′W	687
D07_006	**30°51.020′S**	**36°02.119′W**	**681**
D07_006_0			
D09_007	30°47.678′S	35°59.657′W	654
D09_008	**30°47.598′S**	**36°03.129′W**	**647**
D10_002	30°52.076′S	35°59.995′W	701
D10_003	**30°50.334′S**	**36°02.301′W**	**672**

(FeOOH, goethite), calcite ($CaCO_3$), and carbonate fluorapatite ($Ca_5(PO_4,CO_3)_3F$), which is consistent with previous findings reported by Benites et al. [17,23].

The main peak related to calcite is attributed to the [104] crystal plane and corresponds to an interplanar distance ($d_{[hkl]}$) of 3.04 Å. Upon closer examination of this region (3.5–2.7 Å, Fig. 3b), it is observed that the peak is split and shifted towards lower $d_{[hkl]}$ values, indicating the partial substitution of Ca^{2+} ions by smaller cations within the crystalline lattice of calcite [24,25]. It is important to note that the substitution of Ca^{2+} ions by cations with similar ionic radii, such as lanthanides, is not expected to cause any shift in the diffraction peaks.

Discriminating between different MnO_x phases is challenging compared to calcium-bearing mineral phases due to their poor crystallinity and the occurrence of overlapping diffraction peaks associated with distinct minerals. Specifically, the term *7 Å-manganates* in the literature can be attributed, at the very least, to vernadite (7 Å-vernadite), birnessite, or calcophanite. Similarly, *10 Å-manganates* may typify vernadite (10 Å-vernadite), busserite, asbolane, lithiophorite, or todorokite [26].

A 7 Å-manganate is present only in sample D06_018. On the other hand, most of the analyzed samples exhibit 10 Å-manganates, as evidenced by diffraction peaks corresponding to $d_{[hkl]}$ values of 9.63 and 4.76 Å (Fig. 3c) [26]. Except for samples D02_030 and D07_006_0, where diffraction peaks related to distances below 4 Å are predominantly occupied by calcite and CFA contributions, thereby hindering the identification of MnO_x diffraction peaks. These aspects are characteristic of the old generation of crusts in the RGR summit, as described by Benites et al. [17], which contains a greater amount of biogenic particles associated with calcite and magnesian calcite (Mg-calcite) compared to the younger generation.

Sample D07_006_0, extracted from the top of D07_006, represents the second (young) generation of crusts and is enriched in poorly crystalline MnO_x mineral phases, such as vernadite [17]. Vernadite is a layered mineral with a highly disordered c-axis and a turbostratic arrangement [26,27]. The absence of basal planes in the diffractogram of D07_006_0, coupled with the presence of peaks related to 2.45 and 1.42 Å, allows for the unequivocal identification of Fe-vernadite, a mineral formed through the intergrowth of poorly crystalline iron oxyhydroxide (FeOOH) and MnO_x phase [28]. Although

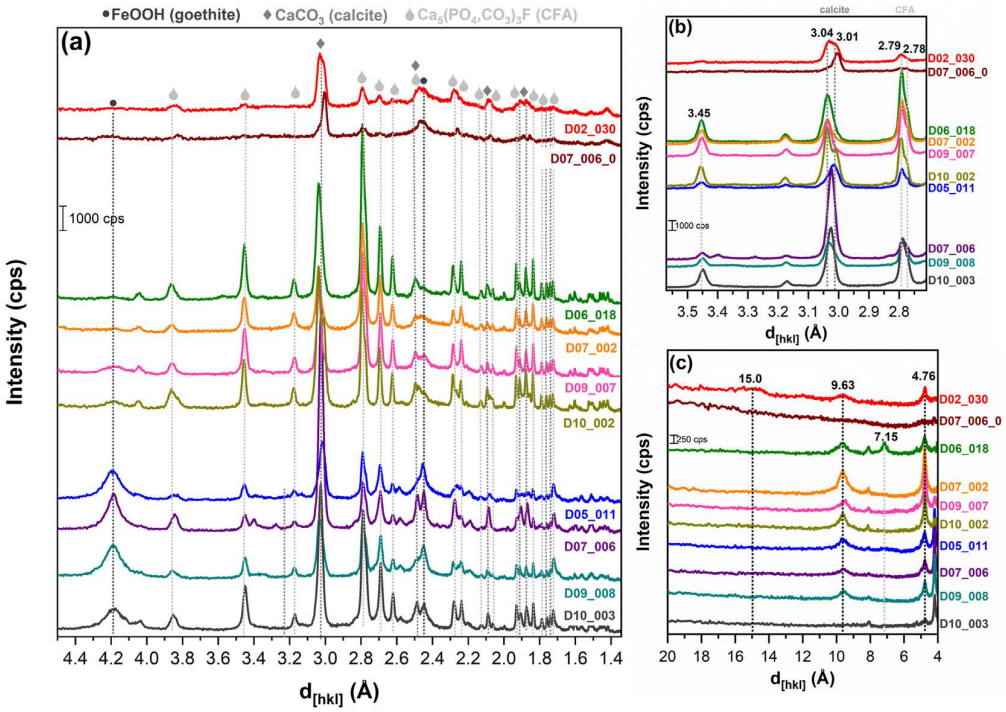

Fig. 3 – X-ray diffractograms of FeMn crust samples (a) and featured regions at 2θ ranges of 25–33° (b) and 2–20° (c).

sample D02_030 seemingly belongs to the 2nd generation, its diffractogram indicates a minor contribution of carbonate and phosphate mineral phases, and the poorly crystalline MnO_x phase exhibits a more ordered structure, resulting in basal diffraction peaks. In this sample, vernadite could be mixed with other phyllomanganates and the peak at 15 Å suggests the presence of an interstratified phase [27].

3.1.2. *Raman spectroscopy*

Given the inherent limitations of relying solely on XRD for the discrimination of all potential MnO_x phases, Raman spectra were acquired from distinct regions of the samples to support the identification of the mineral phases (Fig. 4). However, it is essential to emphasize the tentative nature of spectra attribution in this study. While certain spectral bands may serve as indicators of specific MnO_x phases, their broadened feature can arise from the superposition of numerous narrower bands, thereby hiding phases in lower abundance. Moreover, the available literature on this subject is scarce, with few studies considering the sensitivity of manganese oxides to laser power [29]. In order to mitigate the possibility of laser-induced degradation of MnO_x minerals, different laser powers were examined using D07_006_0 sample (Fig. 4a). Under a laser power of 0.5 mW, the sample remained stable after two acquisitions. However, at 2.5 mW, the relative intensities of the bands were altered, and at 5.0 mW, irreversible broadening of the bands occurred. Consequently, a laser power of 0.5 mW, coupled with an excitation wavelength of 785 nm, was determined to be an optimal condition as it avoids sample degradation and any resultant changes in the spectra that could potentially misguide mineral identification.

The samples belonging to the young crust generation, specifically the uppermost layers of the crusts, exhibit a similar visual appearance, which is reflected in comparable Raman spectra (Fig. 4b). The bands at 639 (strong, *s*), 593 (very strong, *vs*) and around 500 cm^{-1} (medium, *m*) resemble those reported by Manceau et al. [27], which were attributed to Fe-vernadite. The elongated tail of the 639 cm^{-1} band towards the higher wavenumber indicates its superposition with a broad band around 700 cm^{-1}, attributed to poorly crystalized feroxyhyte intergrown with the MnO_x mineral phase. This elongation is more pronounced in sample D07_006_0, for

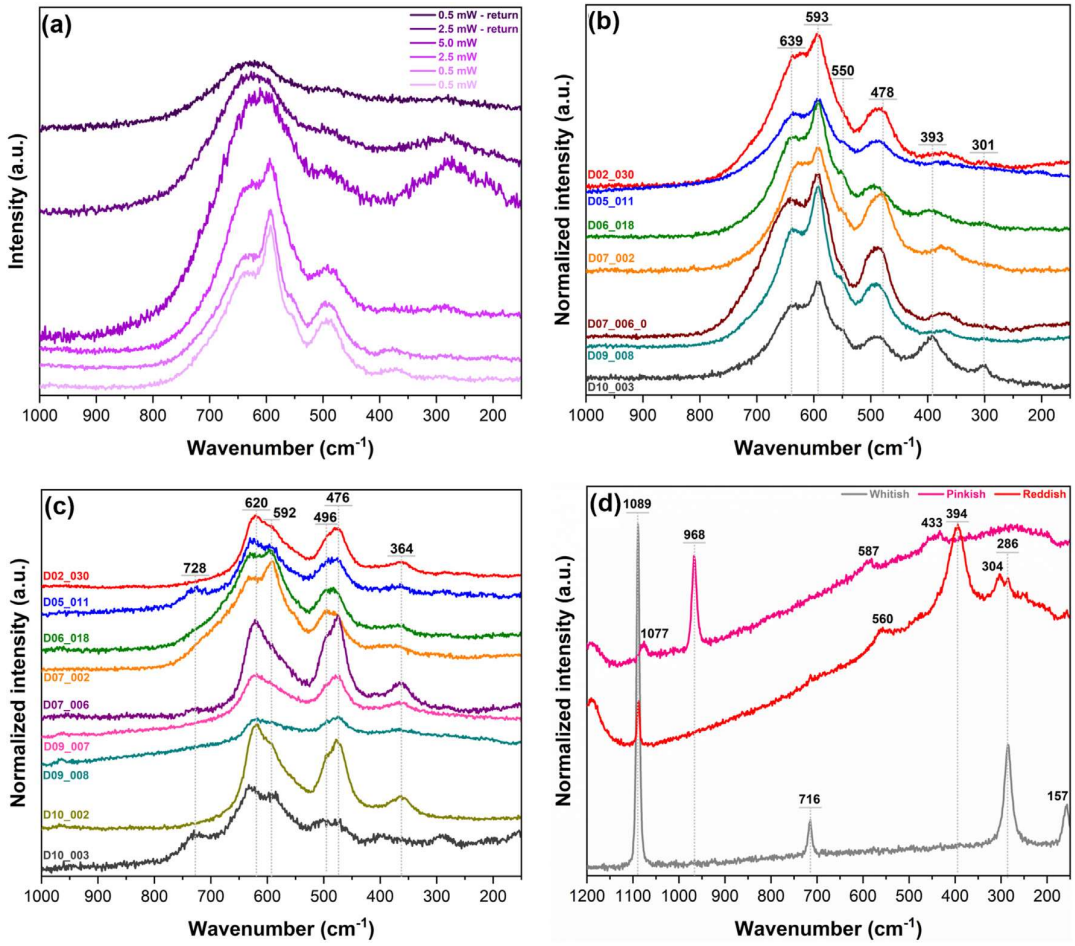

Fig. 4 – Raman spectra of sample D07_006_0 recorded at different laser powers in the same spot (a); Raman spectra of crust layers from the younger (b) and the older generation (c); and of distinct accessory minerals in sample D09_008 (d).

which the XRD data suggest a mineralogical composition primarily consisting of Fe-vernadite. However, the presence of a shoulder (sh) at around 550 cm^{-1} indicates the overlapping of the Fe-vernadite and asbolane spectra [30]. In fact, Novikov et al. [31] claim that the sorption of Ni and Co cations onto vernadite results in its post-depositional conversion to asbolane. In the case of sample D10_003, which has a young crust generation overlying an ironstone layer, the Raman spectrum shows bands at 393 cm^{-1} (*m*) and 301 cm^{-1} (weak, *w*), attributed to vibrational modes of the goethite lattice [32].

Concerning the first-generation crust layers, their older age likely resulted in more extensive post-depositional modifying processes. Consequently, these layers are more heterogeneous than their young counterparts, not only due to the presence of phosphatized minerals but also due to the diversification of MnO_x phases (Fig. 4c). It is worth mentioning that due to this heterogeneity, the collected spectra do not represent the entire sample but rather a specific point. Additional spectra collected for each sample are presented in the Supporting Information (Fig. S4).

Compared to the spectra of the young crust layers (Fig. 4b), the spectra of certain old crust layers exhibit a shifted band at 630 to 620 cm^{-1}, a change in the intensity ratio of bands at 620 and 593 cm^{-1}, and an increased relative intensity of bands around 500 cm^{-1}. These features suggest that vernadite and asbolane may not be the dominant manganate minerals in the old crust layers. The spectra of samples D02_030, D05_011, D07_006, D09_007, D09_008, and D10_002 (Fig. 4c) indicate the superposition of bands originating from the minerals lithiophorite and todorokite. The high relative intensity of bands at 476 and 496 cm^{-1} (*vs*), accompanied by a higher intensity of the 364 cm^{-1} band (*w*) suggests the presence of lithiophorite [33], while the profile between 800 and 500 cm^{-1} resembles that of todorokite, as reported by Bernardini et al. and Mulè et al. [29,33]. Post et al. [30,34] found that a band between 725 and 740 cm^{-1} in the spectra of MnO_x minerals can be associated with the presence of tunnel structures, also known as tectomanganates. In fact, for some of the aforementioned spectra (D05_011, D07_006, and D10_003), a band at 728 cm^{-1} confirms the presence of the tectomanganate todorokite.

The spectrum of sample D06_018 (Fig. 4c) shows equivalent intensities of bands at 629 and 592 cm^{-1} and broader overlapped bands at 496 and 476 cm^{-1} which may be associated with vernadite and birnessite minerals [33]. Considering that vernadite can be assumed as a nanocrystalline and *c*-axis disordered birnessite, the gradual conversion from the former structure to the latter is expected. Over time, the aging of minerals through Ostwald ripening can lead to structures with larger crystallite sizes [35]. On the other hand, the spectrum of D07_002 is similar to those from the 2nd generation crusts (Fig. 4b), showing a very strong band at 592 cm^{-1} and a shoulder at approximately 550 cm^{-1}, corresponding to a mixture of vernadite and asbolane. Lastly, the spectrum of sample D10_003 exhibits broad bands at 728 (w), 633 (vs), 588 (s), and around 500 cm^{-1} (w), possibly related to birnessite and todorokite. The presence of tectomanganates (*i.e.* todokorite) in the old crust layers reinforces the extensive post-depositional modifications favored by the aging of the crusts. According to Wegorzewski et al. [36], todorokite was identified in older FeMn nodules buried below a 530–985 cm sediment column but not in samples closer to the seabed (14–16 cm). Likewise, Wu et al. [37–39] have shown that the conversion of phyllomanganates to tectomanganates depends on geochemical conditions (such as pH, adsorbed or incorporated cations, etc.) that drive structural and chemical transformations. For example, high contents of Co and Ni can lead to the conversion of vernadite to asbolane instead of tectomanganates, which may have occurred in the young crust layers reported herein (Fig. 4b).

In addition to manganese oxides, Raman spectroscopy can also be used to identify accessory minerals present in FeMn crusts. To demonstrate this, spectra were collected from regions of sample D09_008 that exhibited visually distinct colors other than the characteristic black-brownish color of MnO_x minerals, such as whitish, reddish, and pinkish regions (Fig. 4d). The spectrum of the whitish region of the sample displays bands at 1089 (vs), 716 (w), 286 (m), and 157 (w) cm^{-1}, which correspond to Mg-calcite [40]. This finding supports the isomorphic substitution of Ca^{2+} into the calcite lattice as indicated by XRD data (Fig. 3b). However, it is important to highlight that this spectrum represents a specific region and does not represent the entire sample, meaning that possible substitution of Ca^{2+} by larger cations such as Sr^{2+} and Ba^{2+} or other cations with similar ionic radii, such as REE^{3+}, in other regions cannot be ruled out. In addition to bands related to calcite, the spectrum of the reddish region shows bands at 560 (vw), 394 (s), and 304 (w) cm^{-1}, which are attributed to goethite and are in agreement with the XRD data of ironstones from RGR [23]. The spectrum of the pinkish region provides evidence of CFA due to bands at 1077 (w), 968 (s), 587 (vw), and 433 (vw) cm^{-1} [41–43]. Although bands attributed to the vibrational modes ν_3 of phosphate and ν_1 of carbonate can occur around 1040–1080 cm^{-1} [44], the position of the band at 1077 cm^{-1} indicates the insertion of carbonate into the apatite lattice. Therefore, Raman spectra support the mineralogical composition of FeMn crusts suggested by XRD, but it serves as a crucial tool to complement the understanding of MnO_x phases and provide evidence about ionic substitutions into calcite and CFA minerals.

3.2. *Chemical characterization*

3.2.1. *Mass balance of main constituents of FeMn crusts*

From a stoichiometric perspective, elemental substitutions into mineral lattices do not significantly contribute to the mass balance of the main constituents of FeMn crusts. Therefore, the major elemental contents (Table S1) – Mn, Fe, Ca, and P - determined by XRF spectrometry were used to estimate the mass percentage distribution of calcite, CFA, FeOOH, and MnO_x phases in the samples, normalized to 100% (Fig. 5). In this analysis, asbolane ($Ca_{0.1}[Ni_{0.3}Co_{0.1}Mn_{1.5}O_{1.5}(OH)_2]\cdot 0.6\ H_2O$) [45] was considered as the major MnO_x phase in the samples, except for D07_006_0, where vernadite ($Ca_{0.1}Na_{0.1}[Mn_{0.6}Fe_{0.2}O_{1.5}(OH)_{0.5}]\cdot 1.4\ H_2O$) [45] was adopted. Ca was distributed between pure calcite ($CaCO_3$) and CFA ($Ca_5(PO_4)_{2.5}(CO_3)_{0.5}F$). Goethite was used as a representative of Fe minerals, including both goethite and feroxyhyte.

Consistent with the discussion in Section 3.1, samples D02_030 and D07_006_0 predominantly consist of MnO_x. Conversely, the older crust layers present a significant

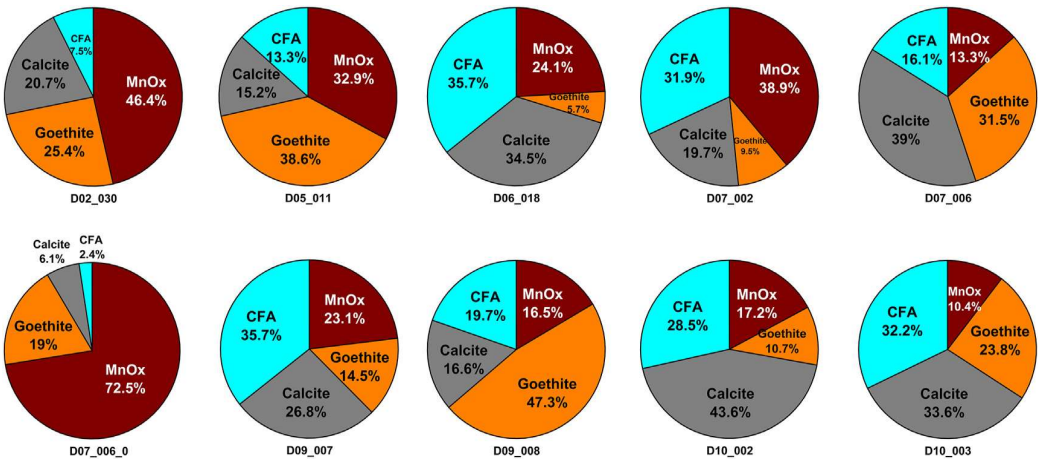

Fig. 5 – Mass percentage (%wt) of main constituents of samples.

amount of calcite and CFA, reflecting a higher accumulation of biogenic particles and phosphatization events [15]. It is important to note that samples D07_006, D10_002, and D10_003 contain fragments of substrate rocks, which can influence the mass balance and result in a decrease in the mass percentage of MnO_x. Samples D05_011, D07_006, D09_008, and D10_003 show thick layers associated with ironstones (Fig. 1) and, as a result, contain a substantial amount of goethite.

3.2.2. *Transition metals and rare earth elements composition*

Interestingly, samples D02_030, D07_002, and D07_006_0 exhibit a higher mass fraction of MnO_x phases, which contain an increased concentration of transition metals and REEs (Fig. 6). Previous research by Benites et al. [17] also observed a higher enrichment of transition metals and REE in the non-phosphatized FeMn crusts (young generation) compared to phosphatized (old generation) ones. This enrichment can be attributed, in part, to a dilution effect caused by the presence of calcite and CFA phases, as the uptake of metals from seawater primarily occurs through adsorption onto MnO_x and FeOOH colloidal particles.

Sample D07_006_0 stands out among the others as a representative of the young generation crusts and exhibits the highest concentration of economically significant metals. Specifically, it contains 0.66 %wt of Co (Fig. 6a; Table S1), which is similar to the average value found by Benites et al. [17] for non-phosphatized RGR FeMn crust samples (6604 ppm), and comparable to FeMn crusts and nodules from the PPCZ (average 6662 ppm) [10]. Furthermore, this value is approximately twice the Co content of crusts from the Atlantic Ocean (3608 ppm) and Indian Ocean (3291 ppm) [10], and more than ten times the Co content of manganese nodules from the Peru Basin (0.048%) [6]. Similarly, sample D02_030, representing the young generation of crusts, also presents a high content of Co (0.51%). These two samples also have the highest concentrations of Ti, Mo, Zr, Nb, and REE elements (except Y) among the analyzed samples (Table S1 and Table S2, Fig. S1).

Sample D07_002, mainly composed of old generation crust with a thin layer of young crust on top, contains the highest amount of Ni (1.12 %wt), Y (345 ppm), and HREE (heavy REE – Tb to Lu, 440 ppm) among the samples analyzed (Fig. 6b; Table S2). In contrast, D07_006_0 has a Ni content of 0.51 %wt and 322 ppm of HREE. The higher concentrations of Y and HREE in D07_002 are possibly due to a more significant presence of CFA phases (Fig. 5). Trivalent Y and HREE anions have a similar ionic radius to Ca^{2+} anions in the seven-fold coordinated position in the CFA lattice, 1.06 pm [46], which favors their isomorphic substitution. This substitution is facilitated by the charge compensation through the substitution of trivalent PO_4^{3-} by divalent CO_3^{2-} anions [47]. The enrichment of Ni might be associated with the mechanism of uptake and subsequent structural incorporation of Ni^{2+} species. The young generation crusts are composed of poorly-crystalline MnO_x with a high density of structural defects, allowing them to adsorb labile species. In contrast, in the older generation crust layers, post-depositional processes can lead to the substitution of Mn^{n+} ($n = 3$ or 4) ions by Ni^{2+} species [48]. Although D07_002 contains a young crust layer, most of its volume consists of older phosphatized layers that can carry a higher content of structurally immobilized Ni. Sample D09_007 presents a similar structure (Fig. 1) and is the second sample in the set with higher Ni content (0.62 %wt).

3.2.3. *Correlation between elements*

Through the obtained results, the correlation between pairs of elements was assessed using a Spearman correlation matrix as presented in Table S3. Scatter plots highlighting moderate ($0.4 < R < 0.59$), strong ($0.6 < R < 0.79$), and very strong ($R > 0.8$) correlations [49] are presented in Fig. 7. For instance, a very strong positive correlation is observed between Co and Mn (Fig. 7a). Furthermore, Co exhibits a strong negative correlation with Ca ($R = -0.721$), supporting its association with manganates. During the formation of FeMn crusts, Co^{2+} cations are adsorbed by negatively charged colloidal MnO_2 particles and subsequently incorporated into the MnO_x structure [11]. Therefore, the high content of Co in the analyzed samples suggests its structural incorporation into asbolane-like minerals, in addition to its adsorption onto vernadite surface. Similarly, Ni does not show a correlation with either Ca or Fe,

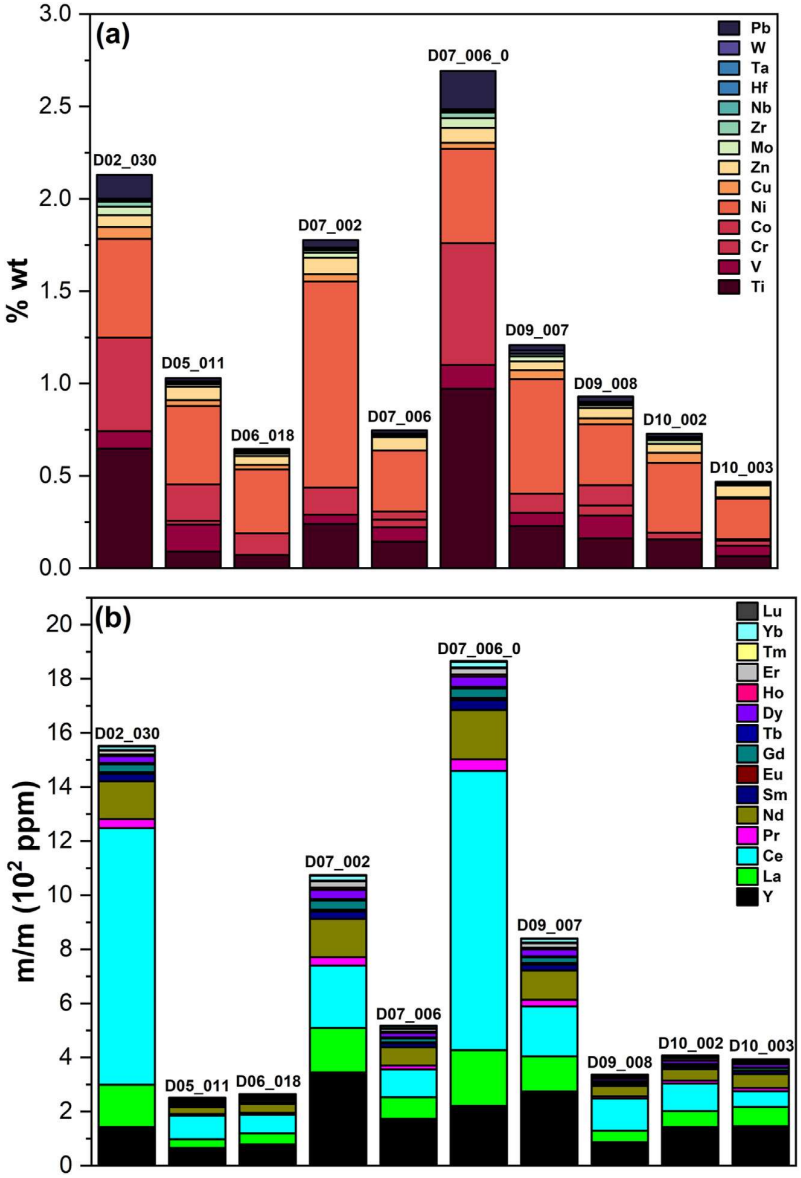

Fig. 6 – Transition metal and lead (%wt) (a) and rare earth elements (ppm) (b) content in the samples.

but it exhibits a strong correlation with manganese (Fig. 7b). Additionally, a moderate correlation between Al and Li is observed (Fig. 7c), indicating their association with lithiophorite, which is consistent with the attributions proposed in Raman spectra (Fig. 4b). Asbolane and lithiophorite are commonly found together in Mn ores and can also be intrinsically mixed into intermediate mineral phases [50].

Among the REE, Ce is the only chemical element that presents a correlation with Mn (Fig. 7d). This strong ($R = 0.697$) and positive correlation can be attributed to the mechanism of Ce uptake from seawater. The electrochemical oxidation of Ce^{3+} to Ce^{4+} facilitates its incorporation into hydrogenetically formed manganates [6]. Previous literature indicates that hydrogenetic crusts (e.g., D02_030 and D07_006_0) and phosphatized crusts (most samples) exhibit Ce enrichment and depletion, respectively, relative to other REEs [10]. Indeed, D02_030 and D07_006_0 demonstrate higher Ce concentrations (Table S2). Most of the REEs show a very strong positive correlation with Ti, such as the example of Ce (Fig. 7e) and La (Fig. 7f). Conversely, Ti demonstrates a strong correlation with Mn (Fig. 7g), although $Ti(OH)_4$ in seawater is captured by FeOOH colloidal particles during crust formation [11]. Therefore, while these correlations may not represent direct mineral associations, the Ti content in FeMn crusts can serve as an indicator of REE content in the samples.

In addition to the correlation with Ti, the REEs exhibit very strong correlations among themselves. For example, correlations between La and Eu (Fig. 7h), as well as between La and Nd (Fig. 7i). This behavior can be explained by the chemical

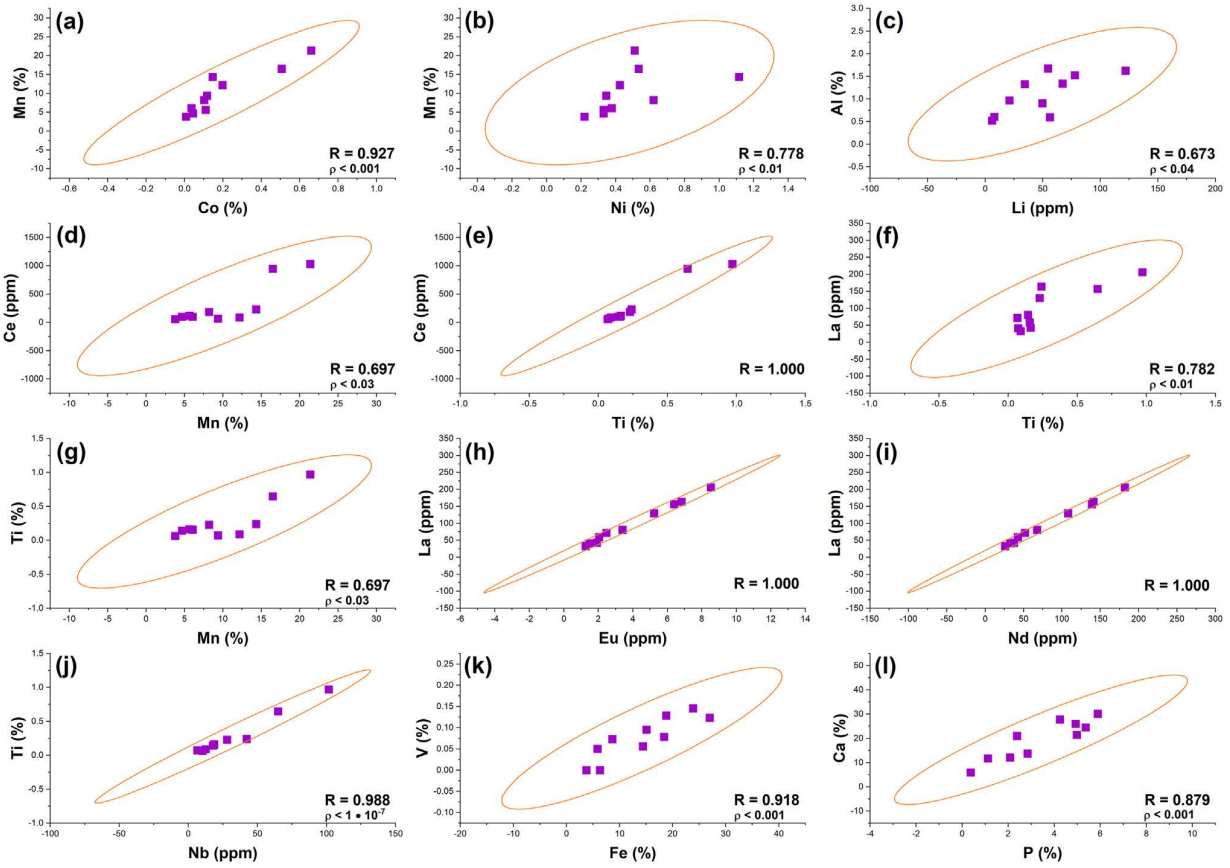

Fig. 7 – Scatter plots showing Spearman correlation between some chemical elements at 95% confidence level as indicated by colored ellipses. R-values are validated for $\rho < 0.05$.

properties of the REEs, wherein similar oxidation states and ionic radii lead to equivalent bond energies and facilitate isomorphic substitution of one element for another within crystal lattices [46,51]. Similarly, Ti demonstrates strong or very strong correlations with Zr (R = 0.939), Nb (Fig. 7j), Mo (R = 0.911), Ta (R = 0.830), and Pb (R = 0.939) [46,52]. In terms of Fe, it exhibits a strong negative correlation with Ca (R = −0.770) and P (R = −0.758), and a very strong positive correlation with V (Fig. 7k). Fe and V are commonly associated in nature, and there is a possibility of structural incorporation of V substituting Fe within goethite lattice [53]. The negative associations specifically with Ca and P arise due to their presence in the CFA phase (Fig. 7l), which leads to the dilution of iron mineral phases within FeMn crusts. Furthermore, the preferential replacement of Fe oxyhydroxides by CFA, rather than Mn oxides, is a common process during phosphatization [54–56].

3.2.4. *Spatial mineral–element association in the FeMn crusts*

To investigate the elemental correlations and their connection with mineral associations, SEM coupled with EDS mapping was performed on polished sections of fragments from samples D07_002 (Fig. 8), D07_006_0 (Fig. 9), and D10_002 (Fig. 10).

The cross-section of the D07_002 crust fragment exhibits an uneven chemical composition with various textures comprising laminated, botryoidal, and shapeless cement with embedded microfossil shells (Fig. S5). The top of the fragment (Fig. 8a) reveals young thin crust laminae deposited between large columns of the older crust. These laminae contained intercalations of Mn- and Fe-rich layers (Fig. 8b), indicating the intergrowth of MnO_x and FeOOH. The surrounding region is predominantly composed of the CFA phase, as indicated by the overlapping of Ca (blue) and P (red) maps. This region also contained abundant calcite microfossils (blue circles). Inset elemental maps suggest that Mg and Ti are associated with MnO_x and FeOOH, while Al and Si are diffused throughout the sample with localized enrichment. The inner region of the fragment exhibits thicker layers of segregated MnO_x, FeOOH, and CFA (Fig. 8c, blue, orange, and pink). Mg (inset of Fig. 8c) is associated with MnO_x instead of calcite or CFA, which could be attributed to the adsorption of cations present in seawater by colloidal Mn oxide particles [11]. The association of Al and Ni with MnO_x (inset maps) supports the presence of specific mineral phases such as lithiophorite and asbolane, respectively. Si appears to be concentrated in the CFA cement, suggesting a possible substitution of P in the CFA

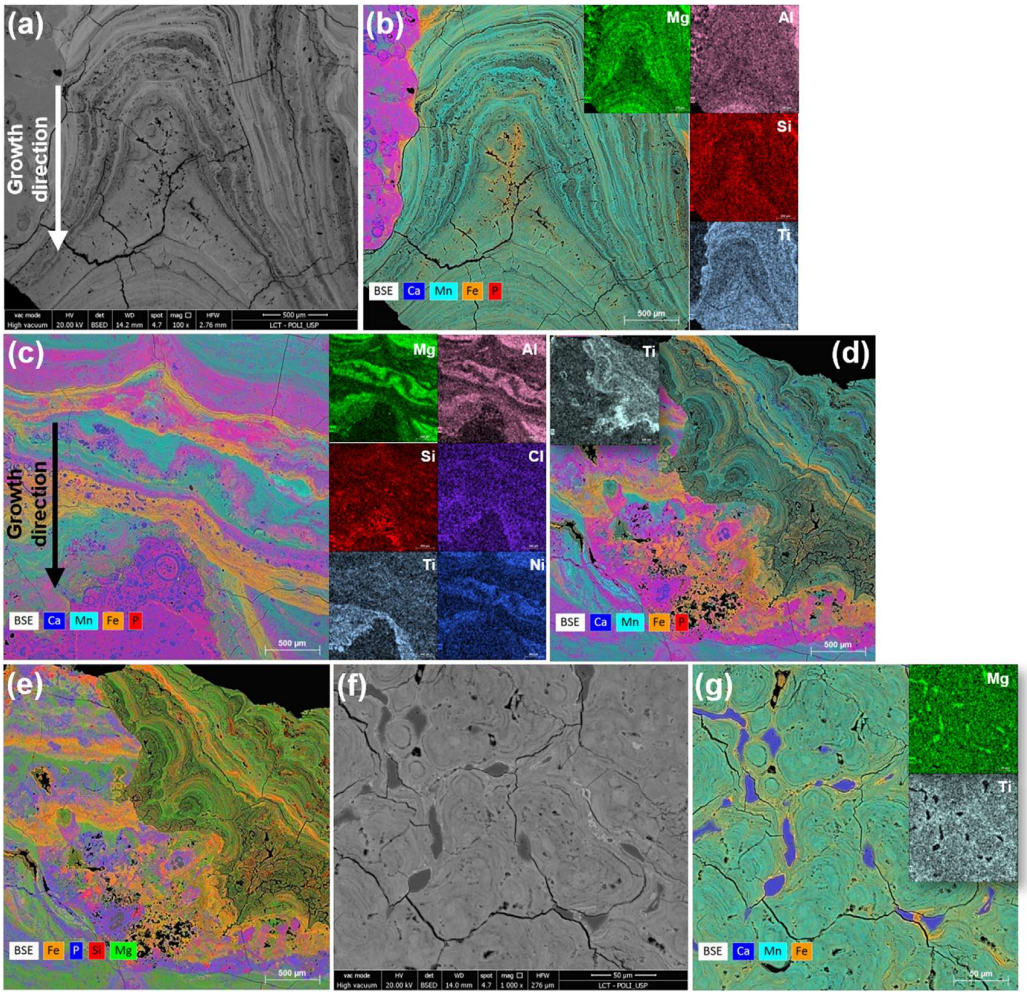

Fig. 8 – SEM micrographs (a) and EDS mapping collected at 100x magnification (b, c, d, and e) of distinct regions from a cross-section of sample D07_002 fragment. SEM micrograph on the top of a fragment of younger crust detached from D07_002 surface (f) and its corresponding EDS mapping (g).

lattice [57]. Cl is uniformly distributed throughout the section, while Ti is concentrated in the arched structure at the top, divided into Fe and Mn phases. Elemental maps in different color schemes (Fig. 8d and e) provide insights into the elemental distribution. This section comprises two distinct generations of crusts separated by a cement of CFA and FeOOH (Fig. S6). The structure of the younger crust generation resembles the one depicted in Fig. 8a, consisting of thin, curved layers of MnO_x and FeOOH phases, forming a botryoidal texture. Towards the lower part of the younger crusts, there is a concentrated region of Mn and Fe with a different texture, possibly indicating the presence of poorly crystallized mineral phases. The inset element map indicates that Ti is predominantly found within the FeOOH mineral phases. Furthermore, the elemental map shown in Fig. 8e provides additional evidence that Mg is associated with MnO_x mineral phases, while Si and P elemental maps do not overlap, supporting the hypothesis of elemental substitution within the CFA lattice.

Fig. 8f displays an electron micrograph of the upper part of a younger crust layer detached from the top surface of sample D07_002. FeMn crust layers exhibit a botryoidal texture arranged around flat, shapeless encrustations of Mg-calcite as depicted in Fig. 8g. The association between Mg and Ca observed in the inset elemental map suggests that, during the aging of the crust, the dissolution of calcite, coupled with phosphatization events, released Mg^{2+} cations that subsequently reprecipitated into MnO_x minerals. EDS data further confirm the association of Ti with FeOOH phase, which is concentrated at the boundary of the Mg-calcite particles. One possible explanation for this phenomenon is the interaction between goethite or feroxyhyte with carbonate anions within calcite, forming robust hydrogen bonds that bind the mineral phases together.

Among all the samples, D07_006_0 best represents the younger generation of FeMn crusts. Similar to the previous findings (Fig. 8f), it also exhibits a botryoidal texture surrounding regions containing Mg-calcite (Fig. 9a and b).

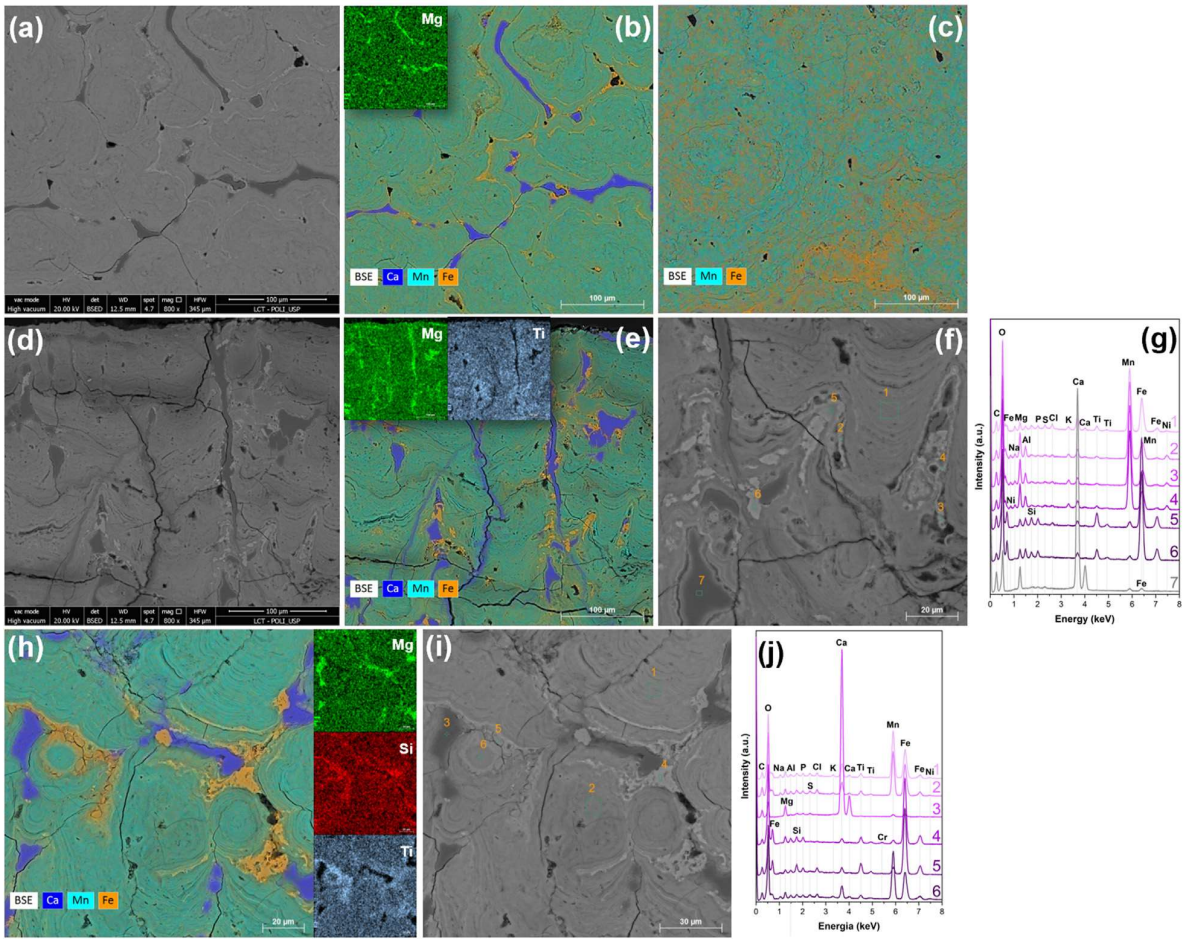

Fig. 9 – SEM micrograph (a) and EDS mappings on the top (b, c) of a fragment from D07_006_0. SEM micrograph (d), EDS mapping (e), and punctual EDS analysis (f, g) on the cross-section of a fragment from D07_006_0. EDS mapping (h) and punctual EDS analysis (i, j) on the bottom of a fragment from D07_006_0.

However, it also displays areas with a more uniform texture that lacks calcite (Fig. S7) and consists of Mn and Fe dispersed within a shapeless matrix (Fig. 9c). It is hypothesized that these regions represent young crusts containing smaller particles of manganese oxide (MnO_x) and iron oxyhydroxide (FeOOH). When observed from a lateral view, the crust layers exhibit a laminated texture (Fig. 9d), with flat, shapeless inclusions in darker regions and some poorly ordered cement without a defined structure. The corresponding elemental mapping (Fig. 9e) shows similarities to the inclusions composed of Mg-calcite surrounded by thin layers of Ti-concentrated FeOOH and enveloped by laminated phases of MnO_x and FeOOH. Even the region with an undefined texture is attributed to the FeMn crust. Point analyses using energy-dispersive X-ray spectroscopy (EDS) (Fig. 9f and g) reveal that regions enriched in Mn (points 2, 3, and 4) are also enriched in Na, Mg, Al, and Ni, indicating their association with MnOx minerals. Similarly, there is a comparable trend between Fe and Ti (points 5 and 6), supporting their mineral association. Point 7 is located in the center of Mg-calcite, and the spectrum shows the absence of a significant amount of P, which is a characteristic feature of the younger crust layer.

The bottom section of the crust exhibits the same structure (Fig. S8) and chemical composition as the top section (Fig. 9h). Additionally, regions rich in FeOOH show concentrated Ti and Si to a lesser extent. Point EDS analyses (Fig. 9i and j) provide further evidence of a higher Si content associated with Fe (points 4 and 5). It is possible that $Si(OH)_4$ present in seawater binds to colloidal particles of FeOOH through hydrogen bonding and becomes incorporated into the crusts [11].

In contrast to the other samples, D10_002 grew on a substrate rock that was extensively phosphatized and contained abundant microfossils (Fig. S9, Fig. 10a). Within the substrate rock, there are visible occurrences of CFA (pink color in Fig. 10b) both inside and outside the shells. Si is also present in the substrate, possibly resulting from the replacement of P, as previously proposed for the D07_002 sample, or due to the presence of siliceous shells and aluminosilicates. Similar to the other samples, the FeMn laminas contain Mg and Ti, although Mg is also combined with Ca in the microfossil shells. Fig. 10c reveals a distinct region that is richer in Mn and

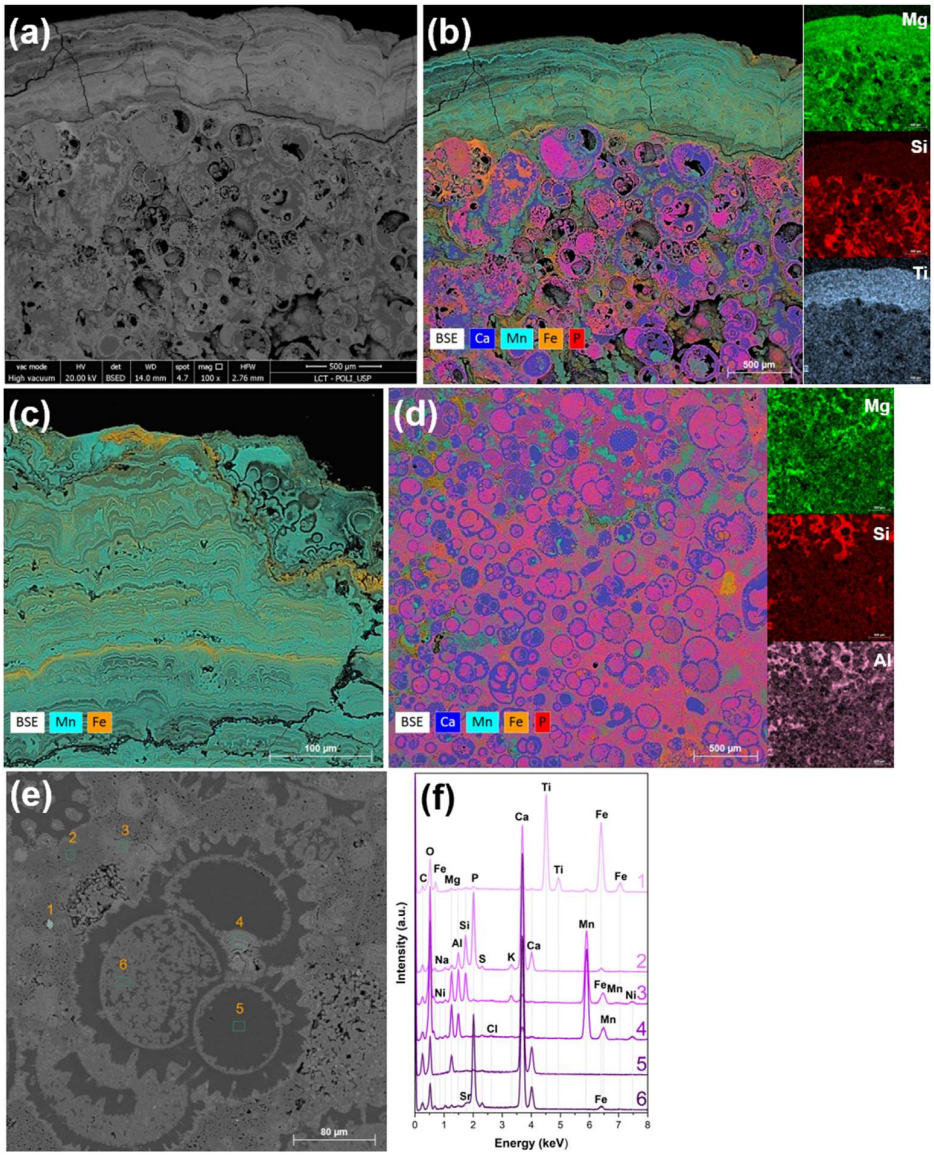

Fig. 10 – SEM micrograph showing FeMn crusts deposited onto a substrate rock (a) and its corresponding EDS mapping (b) in a fragment of sample D10_002. EDS mapping of distinct regions focusing on crusts (c) and substrate rock (d), and punctual EDS analysis of a microfossil structure and surroundings (e, f).

exhibits a more pronounced botryoidal texture, possibly associated with a deposition event separate from the main crust layers. Meanwhile, the substrate rock exhibits a surface enriched in buried microfossils, within a cement composed of CFA and possibly some regions containing aluminosilicates, as indicated by Al and Si elemental mapping (Fig. 10d). Furthermore, many microfossil shell chambers have preserved calcite or Mg-calcite, which could be attributed to phosphatization processes surrounding these chambers, with CFA filling the pores and protecting the pristine calcite from phosphate-rich seawater [15]. Upon closer inspection, it is evident that regions with colloidal FeOOH and MnO_2 have likely penetrated through the pores and contributed to the growth of crusts (Fig. S10). Point analyses using EDS (Fig. 10e and f) reveal a diverse chemical composition. These include small clasts primarily composed of Ti (point 1), cement regions with higher Si and Al content (points 2 and 3), crust deposition containing only MnO_x without associated FeOOH (point 4), shell chambers preserved as Mg-calcite (point 5), and other phosphatized shell chambers containing minor amounts of Sr, which may substitute Ca^{2+} ions in the CFA lattice (point 6).

It is important to note that in all analyzed samples, regardless of the age of the crusts, manganese (Mn) and iron (Fe) minerals are segregated, appearing in distinct laminated or botryoidal arrangements. This is expected since goethite and MnO_x minerals do not have the same crystal structure [28], which favors phase segregation rather than isomorphic

substitution. Therefore, the use of EDS mapping has helped clarify the mineral association of certain minor metallic cations found in FeMn crusts. Titanium (Ti), although correlated with Mn (Fig. 7), is frequently associated with goethite or its precursor mineral, feroxyhyte. Magnesium (Mg), apart from being present in Mg-calcite, is also found in MnO_x phases. These associations are consistent with the hydrogenetic origin of the Rio Grande Rise crusts, as colloidal MnO_x and FeOOH precursors possess surface charges that enable their interaction with ionic species in seawater [11]. Another factor driving these preferential interactions is the ability of FeOOH to establish hydrogen bonds with anionic or neutral species, such as $Ti(OH)_4$. Punctual EDS analysis has also revealed a higher intensity of peaks attributed to Al and Ni associated with MnO_x phases. In particular, this result indicates the presence of relevant mineral phases such as asbolane, lithiophorite, and possible intermediates within the MnO_x fraction. Additionally, the layered structure of these minerals may contribute to the observed laminated textures. The absence of definitive evidence in EDS maps or spectra indicating the association of Co or REEs with any specific phase is due to their low concentration and the high detection limit of EDS, which makes it challenging to detect trace elements dispersed within the mineral matrix. Regarding the REEs, their dispersion among various minerals is consistent with the lack of correlation with Mn, Ca, and Fe (Table S3).

In summary, the main findings of this study are presented in Fig. 11. A structural-chemical approach was employed,

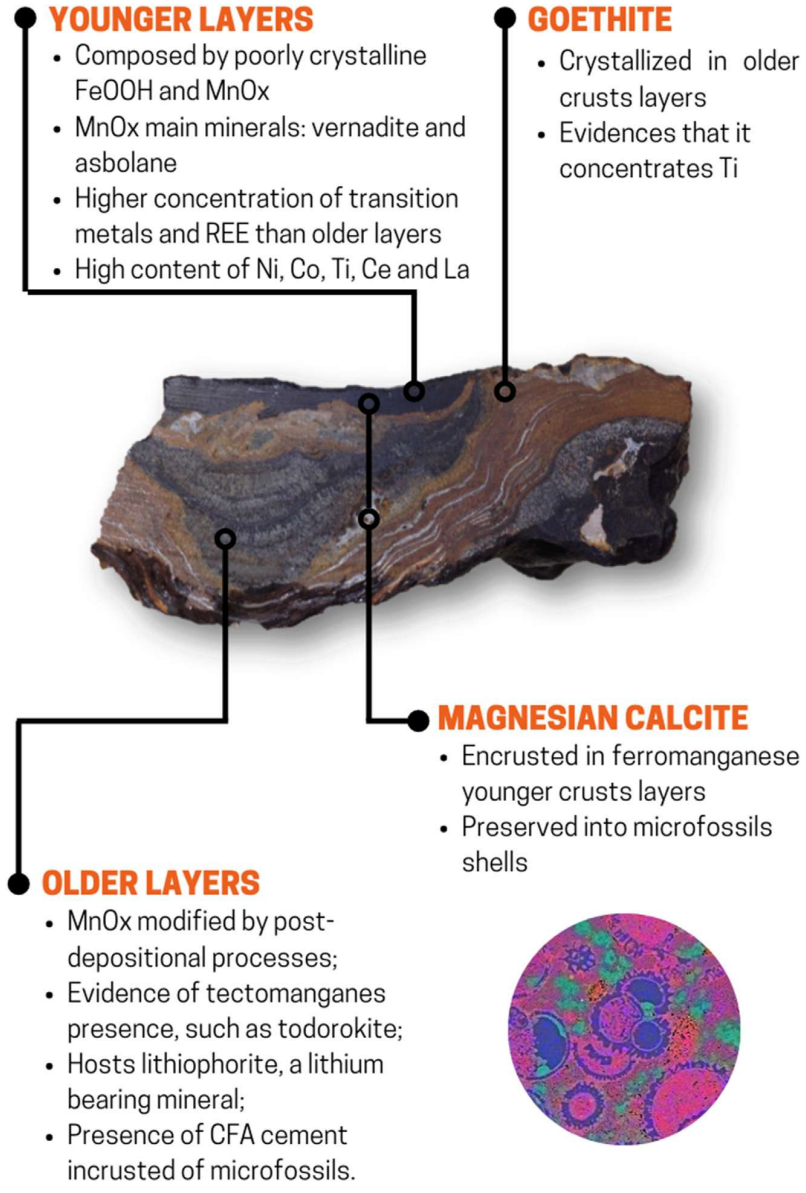

Fig. 11 – Summary of the structural and chemical composition of Fe–Mn crusts analyzed.

utilizing various characterization techniques to investigate the key characteristics of FeMn crusts. The data obtained from the samples collected at the Rio Grande Rise have provided valuable insights that can guide future research and facilitate the planning of FeMn crust exploitation in diverse regions worldwide. These findings serve as a valuable resource for researchers and stakeholders involved in the study and utilization of FeMn crusts.

4. Conclusions

Herein it is reported the application of Raman and SEM-EDS techniques as key characterization tools enabled a more complete mineralogical understanding of the FeMn crusts from the summit of RGR. For instance, 10 Å manganates can be identified as asbolane and lithiophorite, mineral phases that could not be distinguished by the previous study of Benites et al. [17] based only on the PXRD technique. These data have important implications for the element–mineral association.

Taking into account the FeMn crusts as fruitful critical elements reservoirs, structural and chemical characterization shed light on the desirable characteristics of the samples that can be exploited.

- Contain thicker younger hydrogenetic crusts layers bearing higher content of chemical elements of economic interest;
- Have a high content of Ti, considering its strong correlation to REE as well as to valuable transition metals from the 5th (Zr, Nb, and Mo) and 6th (Hf, Ta, and Pb) period of the Periodic Table. These correlations can be especially beneficial for a preliminary *in situ* chemical characterization based on portable XRF techniques aiming to identify the crusts with the biggest potential for exploration.

Additionally, the high level of intergrowth among distinct mineral phases contained in FeMn crusts reveals that any mineral processing aiming at the extraction of metals should appeal to chemical methods/hydrometallurgy (*i.e.*, acid dissolution, selective leaching, etc) rather than physical methods of separation. Thus, the feasibility of commercial exploitation of these samples still lacks much information, including further steps to understand their chemical behavior, environmental and, social impacts.

Declaration of Competing Interest

The authors declare that they have no known competing financial interests or personal relationships that could have appeared to influence the work reported in this paper.

Acknowledgments

This project was funded by Universidade de São Paulo through the Edital de Apoio a Projetos Integrados de Pesquisa em Áreas Estratégicas, PIPAE (2021.1.10424.1.9), by the Fundação de Amparo à Pesquisa no Estado de São Paulo, FAPESP (2016/24946-9) and Conselho Nacional de Desenvolvimento Científico e Tecnológico, CNPq (310566/2022-3). Authors acknowledge Brazilian Research Unity in Astrobiology – NAP/Astrobio, for the use of Raman spectrometer; Laboratório de Química e ICP of Geoanalítica-USP Facility for the ICP-MS analysis; and to the Technological Characterization Laboratory (LCT-USP) staff for samples preparation, X-ray fluorescence, X-ray diffractometry and Scanning Electronic Microscopy collecting data.

Appendix A. Supplementary data

Supplementary data to this article can be found online at https://doi.org/10.1016/j.jmrt.2023.07.021.

REFERENCES

[1] Elshkaki A. Sustainability of emerging energy and transportation technologies is impacted by the coexistence of minerals in nature. Commun Earth Environ 2021;2:186. https://doi.org/10.1038/s43247-021-00262-z.
[2] IEA. World energy outlook 2022, v. 1; 2022. p. 1–524. Paris.
[3] Owen JR, Kemp D, Lechner AM, Harris J, Zhang R, Lèbre É. Energy transition minerals and their intersection with land-connected peoples. Nat Sustain 2022. https://doi.org/10.1038/s41893-022-00994-6.
[4] Lèbre É, Stringer M, Svobodova K, Owen JR, Kemp D, Côte C, et al. The social and environmental complexities of extracting energy transition metals. Nat Commun 2020;11:4823. https://doi.org/10.1038/s41467-020-18661-9.
[5] Franks DM, Keenan J, Hailu D. Mineral security essential to achieving the sustainable development goals. Nat Sustain 2022. https://doi.org/10.1038/s41893-022-00967-9.
[6] Hein JR, Koschinsky A, Kuhn T. Deep-ocean polymetallic nodules as a resource for critical materials. Nat Rev Earth Environ 2020;1:158–69. https://doi.org/10.1038/s43017-020-0027-0.
[7] Milinovic J, Rodrigues FJL, Barriga FJAS, Murton BJ. Ocean-floor sediments as a resource of rare earth elements: an overview of recently studied sites. Minerals 2021;11:142. https://doi.org/10.3390/min11020142.
[8] Bergo NM, Torres-Ballesteros A, Signori CN, Benites M, Jovane L, Murton BJ, et al. Spatial patterns of microbial diversity in Fe-Mn deposits and associated sediments in the Atlantic and Pacific oceans. Sci Total Environ 2022;837:155792. https://doi.org/10.1016/j.scitotenv.2022.155792.
[9] Sakellariadou F, Gonzalez FJ, Hein JR, Rincón-Tomás B, Arvanitidis N, Kuhn T. Seabed mining and blue growth: exploring the potential of marine mineral deposits as a sustainable source of rare earth elements (MaREEs) (IUPAC Technical Report). Pure Appl Chem 2022;94:329–51. https://doi.org/10.1515/pac-2021-0325.
[10] Hein JR, Koschinsky A. Deep-Ocean ferromanganese crusts and nodules. Treatise on Geochemistry 2014;13:273–91. https://doi.org/10.1016/B978-0-08-095975-7.01111-6. Elsevier.
[11] Lusty PAJ, Hein JR, Josso P. Formation and occurrence of ferromanganese crusts: earth's storehouse for critical metals. Elements 2018;14:313–8. https://doi.org/10.2138/gselements.14.5.313.
[12] Benites M, Millo C, Hein J, Nath B, Murton B, Galante D, et al. Integrated geochemical and morphological data provide insights into the genesis of ferromanganese nodules. Minerals 2018;8(1–16):488. https://doi.org/10.3390/min8110488.

[13] Kfouri LO, Millo C, Estela de Lima A, Silveira CS, Sant'Anna LG, Marino E, et al. Growth of ferromanganese crusts on bioturbated soft substrate, Tropic Seamount, northeast Atlantic ocean. Deep Sea Res 1 Oceanogr Res Pap 2021:175. https://doi.org/10.1016/j.dsr.2021.103586.
[14] Park K, Jung J, Park J, Ko Y, Lee Y, Yang K. Geochemical-mineralogical analysis of ferromanganese oxide precipitated on porifera in the Magellan seamount, western Pacific. Front Mar Sci 2023;9:1–11. https://doi.org/10.3389/fmars.2022.1086610.
[15] Benites M, Hein JR, Mizell K, Jovane L. Miocene phosphatization of rocks from the summit of Rio Grande rise, southwest Atlantic ocean. Paleoceanogr Paleoclimatol 2021;36. https://doi.org/10.1029/2020PA004197.
[16] Hein JR, Mizell K. Deep-Ocean polymetallic nodules and cobalt-rich ferromanganese crusts in the global ocean. The united nations convention on the law of the sea, Part XI regime and the international seabed authority: a twenty-five year journey. Brill | Nijhoff; 2022. p. 177–97. https://doi.org/10.1163/9789004507388_013.
[17] Benites M, Hein JR, Mizell K, Blackburn T, Jovane L. Genesis and evolution of ferromanganese crusts from the summit of Rio Grande rise, southwest Atlantic ocean. Minerals 2020;10(1 to 36):349. https://doi.org/10.3390/min10040349.
[18] Amon DJ, Gollner S, Morato T, Smith CR, Chen C, Christiansen S, et al. Assessment of scientific gaps related to the effective environmental management of deep-seabed mining. Mar Policy 2022;138(1–22):105006. https://doi.org/10.1016/j.marpol.2022.105006.
[19] Montserrat F, Guilhon M, Corrêa PVF, Bergo NM, Signori CN, Tura PM, et al. Deep-sea mining on the Rio Grande Rise (Southwestern Atlantic): a review on environmental baseline, ecosystem services and potential impacts. Deep Sea Res Oceanogr Res Pap 2019;145:31–58. https://doi.org/10.1016/j.dsr.2018.12.007.
[20] Sousa IMC, Santos RV, Koschinsky A, Bau M, Wegorzewski AV, Cavalcanti JAD, et al. Mineralogy and chemical composition of ferromanganese crusts from the cruzeiro do sul lineament - Rio Grande rise, South Atlantic. J South Am Earth Sci 2021;108. https://doi.org/10.1016/j.jsames.2021.103207.
[21] Jovane L, Hein JR, Yeo IA, Benites M, Bergo NM, Corrêa PVF, et al. Multidisciplinary scientific cruise to the Rio Grande rise. Front Mar Sci 2019;6. https://doi.org/10.3389/fmars.2019.00252.
[22] Navarro MS, Andrade S, Ulbrich H, Gomes CB, Girardi VAV. The direct determination of rare earth elements in basaltic and related rocks using ICP-MS: testing the efficiency of microwave oven sample decomposition procedures. Geostand Geoanal Res 2008;32:167–80. https://doi.org/10.1111/j.1751-908X.2008.00840.x.
[23] Benites M, Hein JR, Mizell K, Farley KA, Treffkorn J, Jovane L. Geochemical insights into formation of enigmatic ironstones from Rio Grande rise, South Atlantic ocean. Mar Geol 2022;444:106716. https://doi.org/10.1016/j.margeo.2021.106716.
[24] Titschack J, Goetz-Neunhoeffer F, Neubauer J. Magnesium quantification in calcites [(Ca,Mg)CO3] by Rietveld-based XRD analysis: revisiting a well-established method. Am Mineral 2011;96:1028–38. https://doi.org/10.2138/am.2011.3665.
[25] Littlewood JL, Shaw S, Peacock CL, Bots P, Trivedi D, Burke IT. Mechanism of enhanced strontium uptake into calcite via an amorphous calcium carbonate crystallization pathway. Cryst Growth Des 2017;17:1214–23. https://doi.org/10.1021/acs.cgd.6b01599.
[26] Dixon JB, White GN. Manganese oxides. 2018. p. 367–88. https://doi.org/10.2136/sssabookser7.c11.
[27] Manceau A, Simionovici A, Findling N, Glatzel P, Detlefs B, Wegorzewski AV, et al. Crystal chemistry of thallium in marine ferromanganese deposits. ACS Earth Space Chem 2022;6:1269–85. https://doi.org/10.1021/acsearthspacechem.1c00447.
[28] Manceau A, Combes JM. Structure of Mn and Fe oxides and oxyhydroxides: a topological approach by EXAFS. Phys Chem Miner 1988;15:283–95. https://doi.org/10.1007/BF00307518.
[29] Bernardini S, Bellatreccia F, Municchia AC, Ventura G Della, Sodo A. Raman spectra of natural manganese oxides. J Raman Spectrosc 2019;50:5583. https://doi.org/10.1002/jrs.5583. jrs.
[30] Post JE, McKeown DA, Heaney PJ. Raman spectroscopy study of manganese oxides: layer structures. Am Mineral 2021;106:351–66. https://doi.org/10.2138/am-2021-7666.
[31] Novikov GV, Melnikov ME, Oyu Bogdanova, Drozdova AN, Lobus NV. Mineralogy and geochemistry of Co-bearing manganese crusts from the govorov and volcanologist guyots of the magellan seamounts (Pacific Ocean). Oceanology (Wash D C) 2017;57:716–22. https://doi.org/10.1134/S0001437017050137.
[32] de Faria DLA, Lopes FN. Heated goethite and natural hematite: can Raman spectroscopy be used to differentiate them? Vib Spectrosc 2007;45:117–21. https://doi.org/10.1016/j.vibspec.2007.07.003.
[33] Mulè G, Burlet C, Vanbrabant Y. Automated curve fitting and unsupervised clustering of manganese oxide Raman responses. J Raman Spectrosc 2017;48:1665–75. https://doi.org/10.1002/jrs.5240.
[34] Post JE, McKeown DA, Heaney PJ. Raman spectroscopy study of manganese oxides: tunnel structures. Am Mineral 2020;105:1175–90. https://doi.org/10.2138/am-2020-7390.
[35] Eberl DD, Środoń J, Kralik M, Taylor BE, Peterman ZE. Ostwald ripening of clays and metamorphic minerals. Science 1979;248:474–7. https://doi.org/10.1126/science.248.4954.474. 1990.
[36] Wegorzewski AV, Grangeon S, Webb SM, Heller C, Kuhn T. Mineralogical transformations in polymetallic nodules and the change of Ni, Cu and Co crystal-chemistry upon burial in sediments. Geochim Cosmochim Acta 2020;282:19–37. https://doi.org/10.1016/j.gca.2020.04.012.
[37] Wu Z, Peacock CL, Lanson B, Yin H, Zheng L, Chen Z, et al. Transformation of Co-containing birnessite to todorokite: effect of Co on the transformation and implications for Co mobility. Geochim Cosmochim Acta 2019;246:21–40. https://doi.org/10.1016/j.gca.2018.11.001.
[38] Wu Z, Lanson B, Feng X, Yin H, Qin Z, Wang X, et al. Transformation of Ni-containing birnessite to tectomanganate: influence and fate of weakly bound Ni(II) species. Geochim Cosmochim Acta 2020;271:96–115. https://doi.org/10.1016/j.gca.2019.12.023.
[39] Wu Z, Lanson B, Feng X, Yin H, Tan W, He F, et al. Transformation of the phyllomanganate vernadite to tectomanganates with small tunnel sizes: favorable geochemical conditions and fate of associated Co. Geochim Cosmochim Acta 2021;295:224–36. https://doi.org/10.1016/j.gca.2020.12.021.
[40] Borromeo L, Zimmermann U, Andò S, Coletti G, Bersani D, Basso D, et al. Raman spectroscopy as a tool for magnesium estimation in Mg-calcite. J Raman Spectrosc 2017;48:983–92. https://doi.org/10.1002/jrs.5156.
[41] Antonakos A, Liarokapis E, Leventouri T. Micro-Raman and FTIR studies of synthetic and natural apatites. Biomaterials 2007;28:3043–54. https://doi.org/10.1016/j.biomaterials.2007.02.028.
[42] Zhukova IA, Stepanov AS, Korsakov AV, Jiang S. Application of Raman spectroscopy for the identification of phosphate

minerals from REE supergene deposit. J Raman Spectrosc 2022;53:485–96. https://doi.org/10.1002/jrs.6213.
[43] Chakhmouradian AR, Reguir EP, Zaitsev AN, Couëslan C, Xu C, Kynický J, et al. Apatite in carbonatitic rocks: compositional variation, zoning, element partitioning and petrogenetic significance. Lithos 2017;274–275:188–213. https://doi.org/10.1016/j.lithos.2016.12.037.
[44] Awonusi A, Morris MD, Tecklenburg MMJ. Carbonate assignment and calibration in the Raman spectrum of apatite. Calcif Tissue Int 2007;81:46–52. https://doi.org/10.1007/s00223-007-9034-0.
[45] Pohwat P. DANA'S new mineralogy. vol. 85. 8th ed. New York: John Wiley & Sons; 1997.
[46] Shannon RD. Revised effective ionic radii and systematic studies of interatomic distances in halides and chalcogenides. Acta Crystallogr A 1976;32:751–67. https://doi.org/10.1107/S0567739476001551.
[47] Ren J, Liu Y, Wang F, He G, Deng X, Wei Z, et al. Mechanism and influencing factors of REY enrichment in Deep-Sea sediments. Minerals 2021;11:196. https://doi.org/10.3390/min11020196.
[48] Peacock CL, Sherman DM. Crystal-chemistry of Ni in marine ferromanganese crusts and nodules. Am Mineral 2007;92:1087–92. https://doi.org/10.2138/am.2007.2378.
[49] Zhao G, Ding W, Tian J, Liu J, Gu Y, Shi S, et al. Spearman rank correlations analysis of the elemental, mineral concentrations, and mechanical parameters of the Lower Cambrian Niutitang shale: a case study in the Fenggang block, Northeast Guizhou Province, South China. J Pet Sci Eng 2022:208. https://doi.org/10.1016/j.petrol.2021.109550.
[50] Burlet C, Vanbrabant Y. Study of the spectro-chemical signatures of cobalt-manganese layered oxides (asbolane-lithiophorite and their intermediates) by Raman spectroscopy. J Raman Spectrosc 2015;46:941–52. https://doi.org/10.1002/jrs.4755.
[51] Sousa Filho PC de, Serra OA. Terras raras no Brasil: histórico, produção e perspectivas. Quim Nova 2014;37:753–60. https://doi.org/10.5935/0100-4042.20140121.
[52] Fleischer M, Murata KJ, Fletcher JD, Narten PF. Geochemical association of niobium (columbium) and titanium and its geological and economic significance. 1952.
[53] Kaur N, Singh B, Kennedy BJ, Gräfe M. The preparation and characterization of vanadium-substituted goethite: the importance of temperature. Geochim Cosmochim Acta 2009;73:582–93. https://doi.org/10.1016/j.gca.2008.10.025.
[54] Hein JR, Yeh H-W, Gunn SH, Sliter WV, Benninger LM, Wang C-H. Two major cenozoic episodes of phosphogenesis recorded in equatorial pacific seamount deposits. Paleoceanography 1993;8:293–311. https://doi.org/10.1029/93PA00320.
[55] Koschinsky A, Stascheit A, Bau M, Halbach P. Effects of phosphatization on the geochemical and mineralogical composition of marine ferromanganese crusts. Geochim Cosmochim Acta 1997;61:4079–94. https://doi.org/10.1016/S0016-7037(97)00231-7.
[56] Benninger LM, Hein JR. Diagenetic evolution of seamount phosphorite. Marine authigenesis: from global to microbial. SEPM (Society for Sedimentary Geology); 2000. p. 245–56. https://doi.org/10.2110/pec.00.66.0245.
[57] Szurkowska K, Kolmas J. Hydroxyapatites enriched in silicon bioceramic materials for biomedical and pharmaceuticalapplications. Prog Nat Sci: Mater Int 2017;27:401–9. https://doi.org/10.1016/j.pnsc.2017.08.009.

View publication stats